2nd Advanced Optical Metrology Compendium

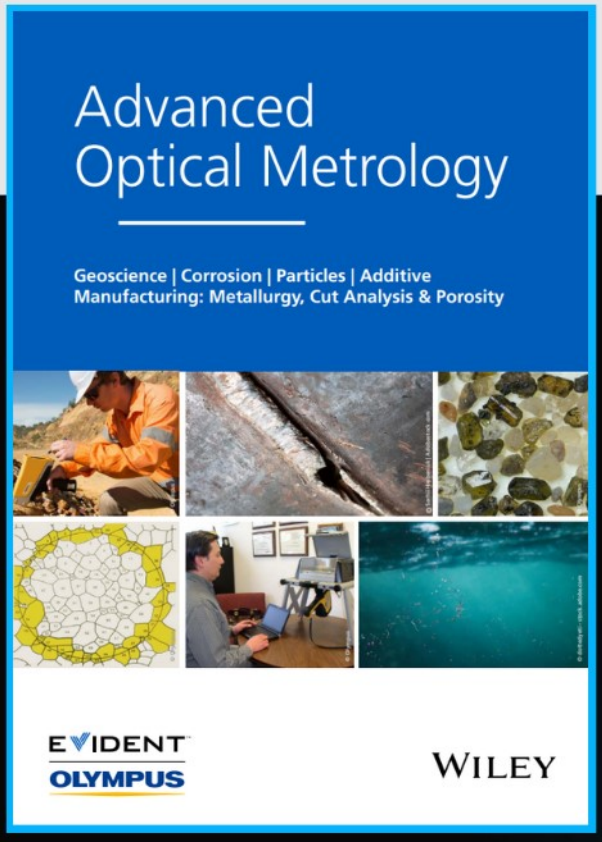

The latest eBook from Advanced Optical Metrology. Download for free.

This compendium includes a collection of optical metrology papers, a repository of teaching materials, and instructions on how to publish scientific achievements.

With the aim of improving communication between fundamental research and industrial applications in the field of optical metrology we have collected and organized existing information and made it more accessible and useful for researchers and practitioners.

EVIDENT
OLYMPUS

WILEY

ADVANCED FUNCTIONAL MATERIALS
www.afm-journal.de

Silane-Mediated Expansion of Domains in Si-Doped κ-Ga_2O_3 Epitaxy and its Impact on the In-Plane Electronic Conduction

Piero Mazzolini, Zsolt Fogarassy, Antonella Parisini, Francesco Mezzadri, David Diercks, Matteo Bosi, Luca Seravalli, Anna Sacchi, Giulia Spaggiari, Danilo Bersani, Oliver Bierwagen, Benjamin Moritz Janzen, Marcella Naomi Marggraf, Markus R. Wagner, Ildiko Cora, Béla Pécz, Abbes Tahraoui, Alessio Bosio, Carmine Borelli, Stefano Leone, and Roberto Fornari*

Unintentionally doped (001)-oriented orthorhombic κ-Ga_2O_3 epitaxial films on c-plane sapphire substrates are characterized by the presence of ≈ 10 nm wide columnar rotational domains that can severely inhibit in-plane electronic conduction. Comparing the in- and out-of-plane resistance on well-defined sample geometries, it is experimentally proved that the in-plane resistivity is at least ten times higher than the out-of-plane one. The introduction of silane during metal-organic vapor phase epitaxial growth not only allows for *n*-type Si extrinsic doping, but also results in the increase of more than one order of magnitude in the domain size (up to ≈ 300 nm) and mobility (highest $\mu \approx 10\ cm^2V^{-1}s^{-1}$, with corresponding lowest $\rho \approx 0.2\ \Omega cm$). To qualitatively compare the mean domain dimension in κ-Ga_2O_3 epitaxial films, non-destructive experimental procedures are provided based on X-ray diffraction and Raman spectroscopy. The results of this study pave the way to significantly improved in-plane conduction in κ-Ga_2O_3 and its possible breakthrough in new generation electronics. The set of cross-linked experimental techniques and corresponding interpretation here proposed can apply to a wide range of material systems that suffer/benefit from domain-related functional properties.

1. Introduction

For almost a decade gallium oxide (Ga_2O_3) has summoned significant interest in the scientific community because of its potential in the field of power electronics.[1,2] This material has five different known polymorphs,[3] all of them characterized by an ultra-wide bandgap of ≈ 5 eV. The monoclinic β-Ga_2O_3 is the thermodynamically stable crystal structure; for this reason, it has been so far the most investigated one with different proposed device architectures, most of them based on homoepitaxy[1] due to the possibility to synthesize bulk β-Ga_2O_3 from the melt.[2,4,5] Moreover, the ability for i) tuning its bandgap through Al- and In-alloying,[6] ii) controlling its electrical properties through *n*-type extrinsic doping (e.g., Si,[7] Sn[8]), and iii) depositing epitaxial layers with low densities of structural defects and smooth surfaces (because

P. Mazzolini, A. Parisini, A. Sacchi, G. Spaggiari, D. Bersani, A. Bosio, C. Borelli, R. Fornari
Department of Mathematical Physical and Computer Sciences
University of Parma
Parco Area delle Scienze 7/A, 43124 Parma, Italy
E-mail: piero.mazzolini@unipr.it

P. Mazzolini, F. Mezzadri, M. Bosi, L. Seravalli, G. Spaggiari, R. Fornari
IMEM-CNR
Parco Area delle Scienze 37/A, 43124 Parma, Italy

Z. Fogarassy, I. Cora, B. Pécz
Centre for Energy Research
Hungarian Academy of Sciences
Institute for Technical Physics and Materials Science
P.O. Box 49, H-1525 Budapest, Hungary

The ORCID identification number(s) for the author(s) of this article can be found under https://doi.org/10.1002/adfm.202207821.

DOI: 10.1002/adfm.202207821

F. Mezzadri
Department of Chemistry
Life Sciences and Environmental Sustainability
University of Parma
Parco Area delle Scienze 17/A, 43124 Parma, Italy

D. Diercks
Shared Instrumentation Facility
Colorado School of Mines Golden
Golden, CO 80401, USA

O. Bierwagen, M. R. Wagner, A. Tahraoui
Paul-Drude-Institut für Festkörperelektronik
Leibniz-Institut im Forschungsverbund Berlin e.V.
Hausvogteiplatz 5–7, 10117 Berlin, Germany

B. M. Janzen, M. N. Marggraf, M. R. Wagner
Institute of Solid State Physics
Technische Universität Berlin
Hardenbergstr. 36, 10623 Berlin, Germany

S. Leone
Fraunhofer IAF
Fraunhofer Institute for Applied Solid State Physics
79108 Freiburg im Breisgau, Germany

of the presence of perfectly matched substrates, i.e., β-Ga_2O_3),[9–12] concurrently has allowed the experimental demonstration of the confinement of 2D electron gases (2DEGs) at β-Ga_2O_3/$Al_xGa_{2-x}O_3$ interfaces.[13] Nonetheless, the low symmetry of the monoclinic cell poses serious obstacles for future device development, i.e., the challenging heteroepitaxial[14,15] as well as homoepitaxial[9,10,16,17] growth of high quality β-Ga_2O_3 thin films and the intrinsic anisotropy of some of its functional properties (e.g., thermal conductivity).[18] For these reasons, other polymorphs of Ga_2O_3 are recently gaining attention. Particularly, κ- (otherwise referred to as ε-) and α-Ga_2O_3 are both considered potential competitors of β-Ga_2O_3 for power electronic applications. Both of these polymorphs in fact have a higher unit cell symmetry with respect to the monoclinic one, which makes them more compatible with relatively cheap crystalline substrates like sapphire. Moreover, for both of these metastable polymorphs a relatively wide window of synthesis parameters have been identified for various physical- as well as chemical- vapor phase epitaxial deposition techniques (PVD and CVD, respectively) that allow for their single phase stabilization.[19]

In particular, orthorhombic κ-Ga_2O_3 possesses a peculiar spontaneous polarization along the (001) direction, predicted to be larger than the one of GaN (23–26 μCcm^{-2}), which should allow for the confinement of high mobility 2DEGs at κ-Ga_2O_3/$Al_xGa_{2-x}O_3$ heterointerfaces characterized by higher carrier densities ($n \approx 10^{14}$ cm^{-2}) with respect to the ones obtainable in β-based heterostructures and in principle without the need of modulation doping.[20–22] Nonetheless, despite the possibility of depositing high quality (001)-oriented κ-Ga_2O_3/$Al_xGa_{2-x}O_3$ heterostructures on cheap c-plane sapphire substrates, no 2DEG has been so far experimentally reported.[23] This is probably linked to the real structure of this orthorhombic polymorph[24] and in particular to the presence of rotational domains commonly found in heteroepitaxial films despite different employed substrates,[25] with the exceptions of recently reported single domain layers obtained on an epitaxially matched $GaFeO_3$ substrate[26] and on an offcut c-plane sapphire.[27] In fact, epitaxial (001)-oriented κ-Ga_2O_3 thin films are characterized by a peculiar columnar structure with ≈ 10 nm width.[24] This morphology is related to the presence of 120°-rotated orthorhombic κ-Ga_2O_3 domains, that should be nominally free of dangling bonds,[24] and initially caused an erroneous attribution to a pure hexagonal cell of the ε-Ga_2O_3 polymorph. For this reason, both the ε and κ nomenclatures can be found in literature even if referring to the very same polymorph. In this manuscript we refer to the orthorhombic polymorph with the correct κ nomenclature. However, it is not trivial to obtain a fine control of the electrical properties in κ-Ga_2O_3 thin films: to the best of our knowledge, no PVD extrinsically doped κ-Ga_2O_3 electrically conducting layer has ever been reported in literature. On the other hand, CVD deposited layers, and in particular metal-organic vapour phase epitaxy (MOVPE), already demonstrated the possibility to extrinsically dope the material during the deposition process with the employment of a silane (SiH_4) flow, or ex-situ via thermally-induced Sn diffusion.[28] Particularly, in the case of Si, a partial solubility into κ-Ga_2O_3 is expected to take place mostly as Si_{Ga} substitutional in the tetrahedral Ga_3 lattice sites and resulting in a shallow donor state.[29] Nonetheless, the extrinsically doped layers suffered from a limited electron mobility (at room temperature $\mu \approx 1$ $cm^2V^{-1}s^{-1}$) due to a hopping transport mechanism.[28,29] As recently suggested by Kneiß et al.[30] and some authors of this work,[31] this could be linked to the nanometric-sized rotational domains representing an effective barrier for the in-plane electronic conduction, i.e., a perturbation in the lateral crystal periodicity comparable to the electrons' mean free path.[29] Therefore, finding synthesis conditions that could at the same time allow the extrinsic doping of the material and a domain size control would represent a major step forward for the understanding of the real κ-Ga_2O_3 intrinsic material properties, which is in turn fundamental for its breakthrough in the field of new generation electronic devices.

In this article we demonstrate that the typical rotational domain size in electrically conducting Si-doped κ-Ga_2O_3 layers on c-plane sapphire substrates can increase from ≈ 10 to ≈ 300 nm. Particularly, we show that this is closely related to the addition of silane during the MOVPE deposition, which could either increase the mobility of the adsorbed species during growth or decrease the initial nuclei density, resulting in a larger domain formation. Moreover, we provide i) nondestructive characterization techniques and procedures (X-ray diffraction XRD and Raman spectroscopy) that allow relative comparisons of the mean rotational domain size in κ-Ga_2O_3 epitaxial films and ii) a direct experimental proof (i.e., in-plane versus out-of-plane resistance measurements performed on insulated mesa structures with well-defined geometries) that the mean domain dimension is itself playing a fundamental role—in combination with planar defects—in the determination of the in-plane electronic conduction. We believe that these findings are of paramount importance for the full physical understanding of the κ-Ga_2O_3 material system, paving the way for overcoming its defects-driven limitations which have so far inhibited its application in the field of power electronics.

Moreover, the general occurrence of rotational domains in heteroepitaxy is common for the growth of lower symmetry (epilayer) over higher symmetry (substrate) materials. Their presence and size distribution can generally result in significant consequences on the functional properties of the epilayer. In particular, as discussed by Grundmann et al.,[32] the rotational domains could affect the impurity distribution and the concentration of deep levels in the layer, cause reduced carrier diffusion length, mobility and lifetime, or lower the efficiency of radiative recombination; this can in turn detrimentally affect the properties of various devices, e.g., breakdown voltage, leakage current, or quantum efficiency. Apart from the κ-Ga_2O_3 here investigated, also the heteroepitaxy of the β polymorph on c-plane sapphire is affected by the presence of rotational domains that negatively reflects on its functional properties.[14,15] Similarly, in other heteroepitaxial material systems like the orthorhombic $SrRuO_3$ deposited on $SrTiO_3$,[33] $LiNbO_3$ and $LiTaO_3$ on Si,[34] Heusler Ni–Mg–Ga alloys on MgO,[35] or the monoclinic $BiFeO_3$ on $LaSrAlO_4$ and $SrTiO_3$,[36] the domain engineering plays a fundamental role with application fields ranging from spintronics and memory devices, radio-frequency acoustic filters and photonic devices, memory shape alloys and magnetocaloric effect, or piezoelectricity. The experimental approach here proposed combines several nondestructive as well as destructive techniques that could be generally advantageous for the thorough characterization of various

domain-structured epilayers, a key requirement when these structural defects can be considered as functional elements.

2. Results

2.1. X-Ray Diffraction

Figure 1a reports the typical XRD symmetric out-of-plane diffraction pattern obtained for the investigated (001)-oriented κ-Ga_2O_3 layers on c-plane sapphire, which has been found to be qualitatively similar for all the different silane fluxes (i.e., no additional diffraction peaks were identified). The crystal structure is purely orthorhombic and all the deposited thin films are characterized by the presence of 120° in-plane rotated domains as exemplarily shown in Figure 1b by the φ-scan performed on the (122) reflection.[37] For sake of clarity, the four expected peaks associated with each of the three rotational domains were calculated and highlighted (labelled with Roman numbers I, II, and III) in Figure 1b and perfectly match the experimental data. The full width at half maximum in 2θ-θ scans is not significantly affected by the silane flow Φ_{SiH_4} [the mean FWHM for the most intense (004) peak is ≈ 0.057° with scattered variations among the samples below 10%, see Figure S1, Supporting Information]. The incorporation of Si in the κ-Ga_2O_3 matrix should preferably occur as a Ga substitution (Si_{Ga}) in the tetrahedral sites as previously shown via electron paramagnetic resonance.[29] The c unit cell parameter (evaluated from 2θ-θ XRD scans) does not seem to be majorly affected by the Φ_{SiH_4} in our samples: the recorded c variations (between ≈ 9.260 and 9.275 Å) are well in line with previously reported data for the orthorhombic Ga_2O_3 polymorph.[38] This is likely related to the limited amount of provided Si, as well as the non-trivial role of the Si-Ga aliovalent substitution and related defects (see following subsections).

Noteworthy, the increment of the Φ_{SiH_4} provided during the deposition process is also accompanied by a significant reduction of the rocking curve FWHM values [ω-scans of the most intense (004) peak, see Figure 1c], indicating a decrease of the crystal mosaicity with respect to the substrate normal. In particular, a decrease from a maximum of 0.371° (nominally

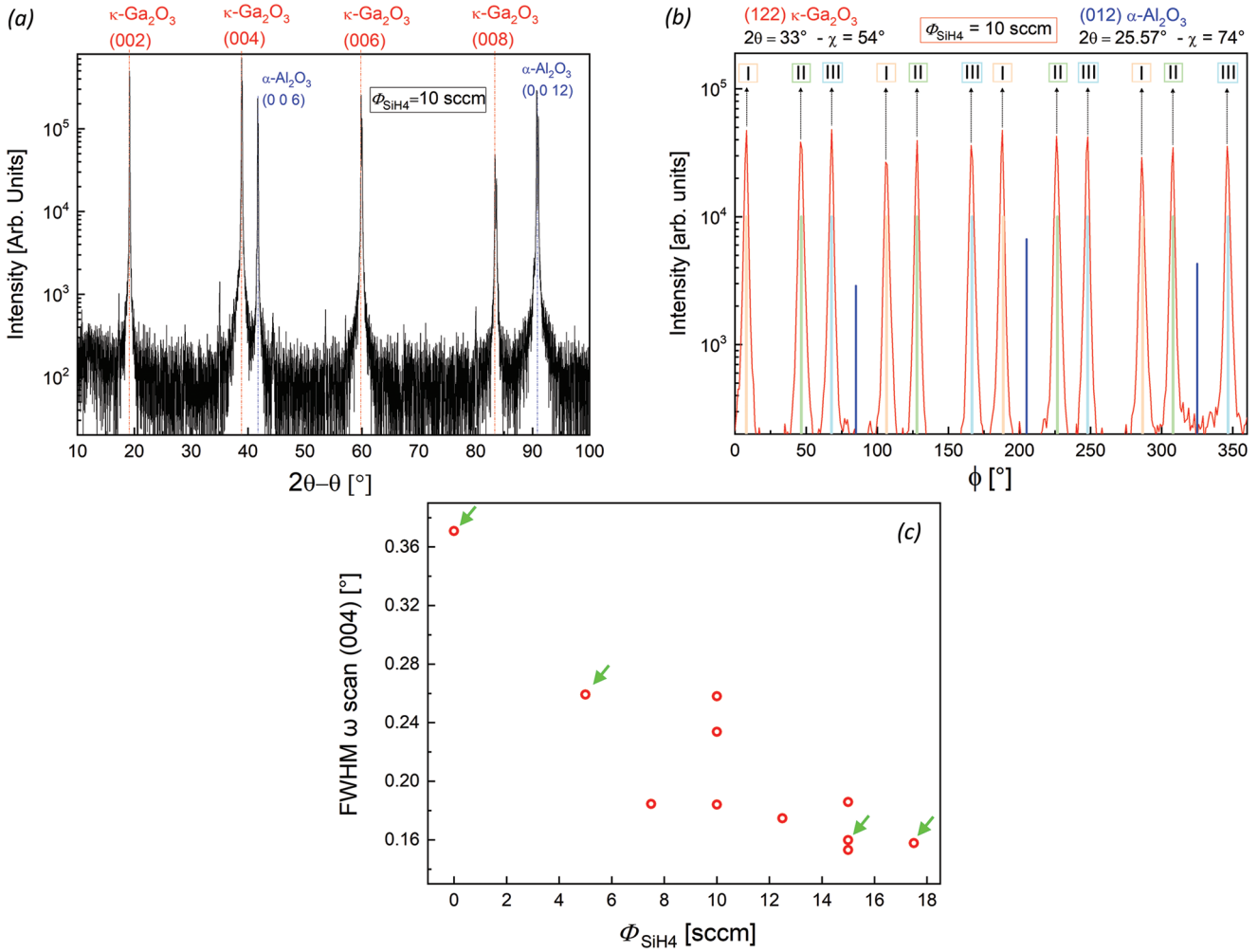

Figure 1. XRD a) 2θ-θ scan and b) φ-scan of a (001) κ-Ga_2O_3 layer deposited on c-plane sapphire with 10 sccm silane flux; in b), the Roman numbers I, II, III, and respective orange, green, and cyan lines refer to the calculated and expected positions for the three 120° rotated domains. c) Full width at half maximum (FWHM) in ω-scans (rocking curve) of the (004) peak as a function of the Φ_{SiH_4}. The green arrows in c) highlight the samples that have been further investigated by TEM.

undoped, i.e., $\Phi_{SiH_4} = 0$) down to a minimum of 0.153° (Φ_{SiH_4} = 15 sccm) is recorded. The displayed set of rocking curve values obtained in these κ-Ga_2O_3 layers deposited with silane (mostly < 0.2° for $\Phi_{SiH_4} \geq$ 7.5 sccm, see Figure 1c) are among the best reported values in literature for this material system, regardless of the presence of an extrinsic dopant/ligand, the employment of different substrates, or various CVD or PVD growth techniques.[23,25,39–44] The only sensibly lower rocking curve value published so far (0.08°) refers to an undoped κ-Ga_2O_3 layer deposited on an offcut c-plane sapphire substrate and referred to as a single-domain.[27] Three selected samples (0, 5, and 15 sccm Φ_{SiH_4}, among the highlighted by green arrows in Figure 1c) were further investigated through XRD reciprocal space mapping (RSM) in the vicinity of the (122) orthorhombic κ-Ga_2O_3 reflection (see Figure S2 and Table S1, Supporting Information). In line with the symmetric out-of-plane measurements of the (004) reflection (Figure 1c), the (122) ω FWHM showed a clear difference between the two Si-doped samples and the nominally undoped one (Table S1, Supporting Information). It should be noted that the [122] direction is ≈ 54° away from the surface normal, so a relevant component of the scattering vector is in-plane. Similarly, the 2θ FWHM values extracted from the RSM measures show a significant reduction as Φ_{SiH_4} is introduced during growth (from 0.667° for the layer without Φ_{SiH_4} to 0.412° and 0.428° for the 5 and 15 sccm samples, see Table S1, Supporting Information).

2.2. In-Plane Transport

Similar to the highlighted trend in the rocking curve values (Figure 1c), also the room-T resistivity ρ shows a pronounced decrease between 0 (≈ 10^3–10^4 Ωcm) and 7.5 sccm Φ_{SiH_4} (≈ 10^{-1} Ωcm), while a further increase of the Φ_{SiH_4} did not result in any other sensitive ρ variations, i.e., ρ plateaus at ≈ 0.5 Ωcm apart from a single value ($\rho \approx 2$ Ωcm) recorded for the highest tested silane flow (Φ_{SiH_4} = 17.5 sccm) (see **Figure 2**a). Particularly, a minimum value of $\rho \approx 0.2$ Ωcm is reached for Φ_{SiH_4} = 15 sccm. The T-dependent (T = 300–50 K) resistivity $\rho(T)$ of the investigated layers points toward the electronic conduction

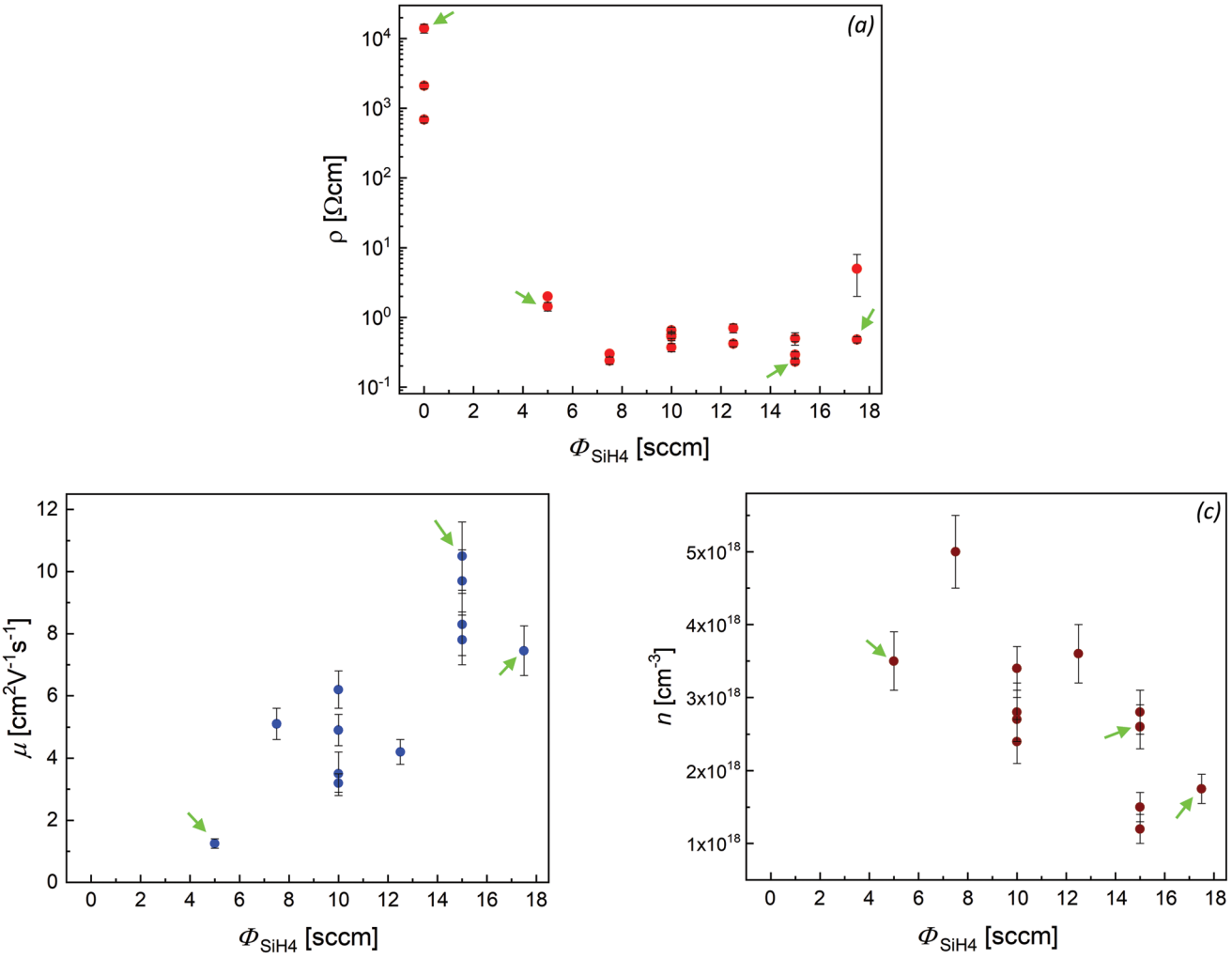

Figure 2. Room temperature, a) electrical resistivity ρ, b) mobility μ, and c) charge carrier density n extracted from van der Pauw–Hall electrical measurements of Si-doped κ-Ga_2O_3 layers as a function of the Φ_{SiH_4} provided during the deposition. The green arrows highlight the samples that have been further investigated by TEM.

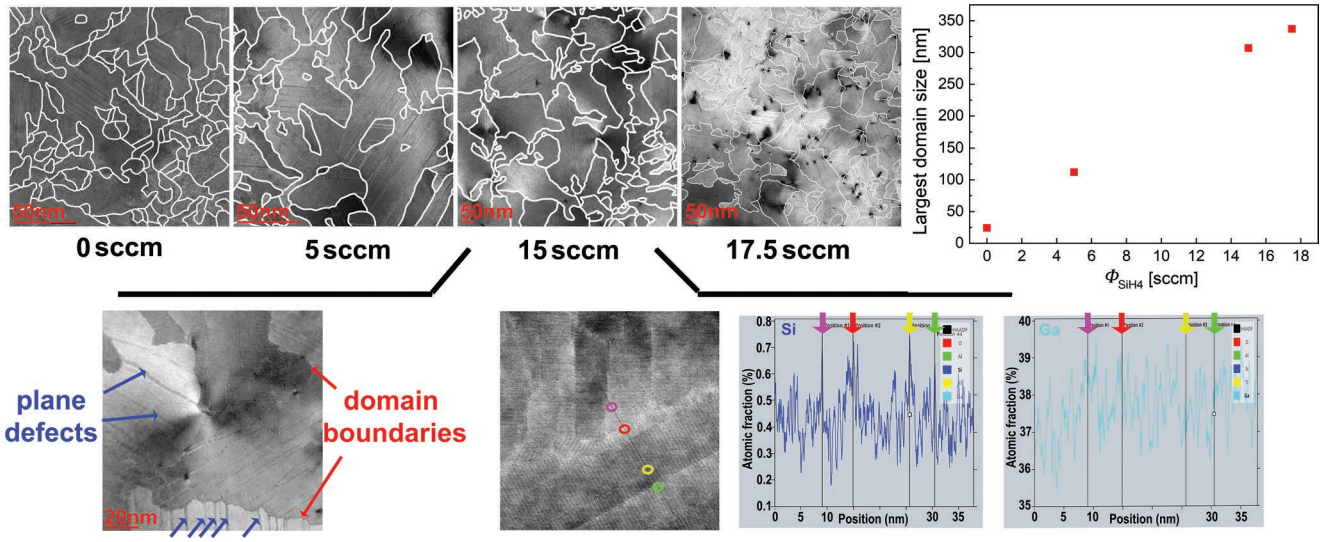

Figure 3. Plan view TEM images of samples deposited at $\Phi_{SiH_4} = 0-5-15-17.5$ sccm. A schematical representation of the typical plane defects identified in top view images is highlighted by blue (inside the domains) and red (domain walls) arrows for the 15 sccm sample. An EDS line profile crossing various extended defects with corresponding Si and Ga concentrations extracted for the same sample is reported; circles and arrows help to identify the corresponding image-to-atomic fraction positions for the presented EDS line profiles.

being dominated by a variable-range hopping transport mechanism (VRH) as previously shown for this material system,[28,29] despite the employment of different Φ_{SiH_4} (Figure S3, Supporting Information). When $\ln(\rho)$ is plotted versus $T^{-0.25}$, i.e., VRH for independent electrons (Mott-VRH),[45] the natural logarithm of ρ shows linear dependencies (Figure S3b, Supporting Information), whose slopes and absolute values significantly decrease from nominally undoped to doped samples. It is worth noting that $\ln(\rho)$ seems to show linear behavior even when plotted versus $T^{-0.5}$ (Figure S3c, Supporting Information), as in VRH for interacting electrons (Efros-Shkolvskii ES-VRH).[45,46] Unfortunately, the variation of the resistivity magnitude along a linear trait is not wide enough to permit to unambiguously distinguish between the two exponents, i.e., ES-VRH or Mott-VRH. Nonetheless, the proximity to the semiconductor to metal transition[29] and going toward higher temperatures[47] should favor the Mott- over the ES-VRH transport mechanism (see Supporting Information for additional details).[48]

Interestingly, the RT mobility μ increases about one order of magnitude while increasing the provided Φ_{SiH_4} (from ≈ 1 up to ≈ 10 $Vcm^{-2}s^{-1}$, Figure 2b). Such mobility values are typical of a transport between localized states, about one-to-two orders of magnitude lower than room-T μ of β-Ga_2O_3 (i.e., in the range of 50 to 100 $Vcm^{-2}s^{-1}$ for β with similar n of about 10^{18} cm^{-3}).[49] The comparison between the monoclinic and the orthorhombic polymorph is relevant due to their similar electron effective masses.[29,50,51] Conversely, the RT n is found to follow an opposite trend with the increment of Φ_{SiH_4}, decreasing from ≈ $3-5\times10^{18}$ down to ≈ 1×10^{18} cm^{-3} while increasing the Φ_{SiH_4} (Figure 2c).

2.3. Transmission Electron Microscopy–TEM

Four selected samples deposited at different silane flows (i.e., $\Phi_{SiH_4} = 0-5-15-17.5$ sccm, highlighted with green arrows in Figure 1c and Figure 2) were further investigated via TEM and EDS. Plan view images (**Figure 3**) confirm that the orthorhombic structure is affected by the presence of 120° rotated domains in all samples (XRD in Figure 1b, TEM Fourier transform patterns in Figure S6, Supporting Information). Of note, the increment of the provided Φ_{SiH_4} results in an evident qualitative enlargement of the domains (Figure 3). Nonetheless, a quantitative assessment of their mean size is not easily achievable due to their irregular shape. Therefore, the area of the domains for each analyzed sample has been evaluated for the reported plan view images in Figure 3. The evaluated areas were translated into regular circles and their diameters were considered as the grain size (full analysis reported in Figure S4, Supporting Information). In line with previous reports,[24] the typical domain size of a nominally undoped sample is ≈ 5 to 20 nm wide. Nonetheless, a clear trend between the maximum domain size and the Φ_{SiH_4} is identified (Figure 3). In particular, the maximum domain size is observed passing from ≈ 20 nm up to ≈ 320 nm for Φ_{SiH_4} of 0 and 17.5 sccm, respectively.

The HRTEM plan view images at higher magnification allow the identification of domain boundaries and plane defects inside the domains (exemplarily highlighted by arrows in a plan image of a 15 sccm layer in Figure 3). EDS line profiles from the TEM plan views allowed for roughly (due to the Si signal being close to the detection limit) estimating the amount of Si with respect to Ga (≈ 1% for Φ_{SiH_4} of 15 sccm, see exemplary line profile scan in Figure 3; Figure S5, Supporting Information). For the 17.5 sccm sample the value was fluctuating over a large range (≈ 2.5–3.5%, Figure S5, Supporting Information). Moreover, the investigated line profiles suggest a slight Si accumulation located in the vicinity of defects, i.e., domain boundaries and plane defects (e.g., red arrow in the EDS line profile of the 15 sccm sample in Figure 3 highlighting a domain boundary). Nonetheless, the possible Si-accumulation on the defect sites is not clearly present in all the investigated line

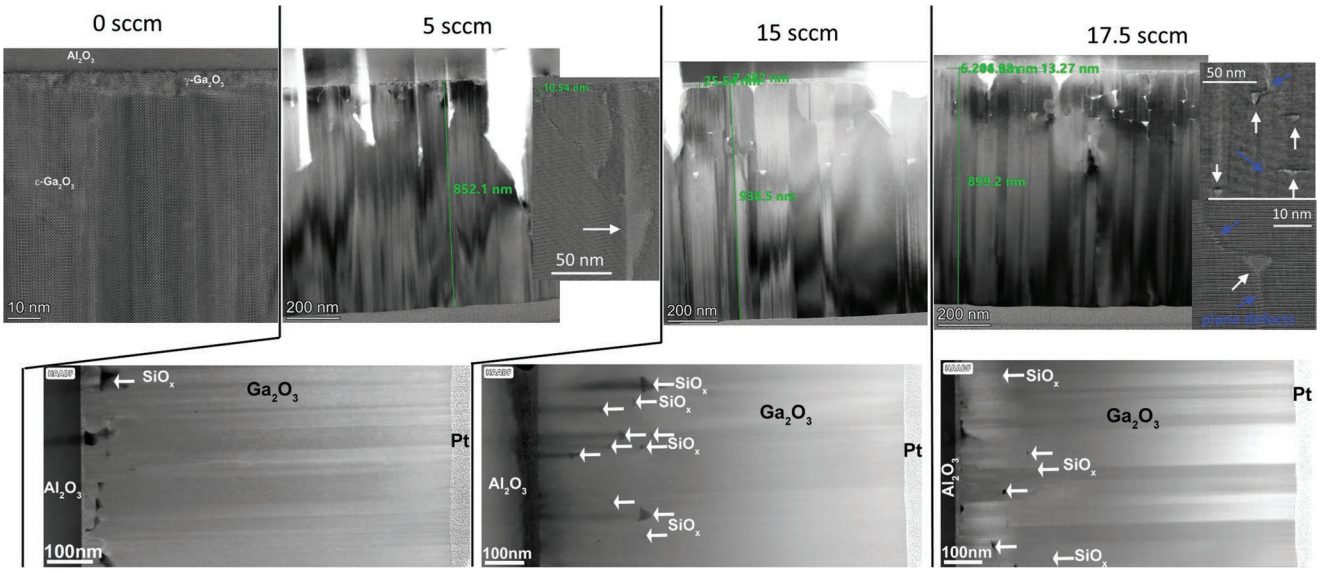

Figure 4. Cross sectional TEM and HRTEM for samples deposited at different Φ_{SiH_4}. The white arrows highlight some of the SiO_x precipitates and blue arrows plane defects located at the apexes of the triangular precipitates.

profiles (e.g., see additional 15 and 17.5 sccm TEM plane scans and EDS line profiles in Figure S5, Supporting Information).

Additional cross-sectional TEM images (**Figure 4**) allowed the identification of a γ-Ga_2O_3 interlayer at the sapphire/κ-Ga_2O_3 interface with an irregular thickness ranging between 2 and 25 nm for all the investigated samples (see Fourier transform patterns of selected interface areas in Figure S6, Supporting Information). The presence of a γ interlayer has been already highlighted for this material/substrate system deposited via MOVPE.[24] Amorphous SiO_x precipitates with a triangular shape were present in all the investigated samples deposited in the presence of a Φ_{SiH_4} (Figure 4; Figure S7, Supporting Information). Interestingly, i) the presence of these precipitates seems to be limited to just the first 200–300 nm of the layer (i.e., closer to the substrate interface) and ii) their mean size diminishes with increasing Φ_{SiH_4} (from ≈ 50 nm down to ≈ 2–5 nm base length for 5 and 17.5 sccm, respectively—see Figure 4), while their density increases.

Moreover, the combined plan-view and cross-sectional TEM investigation shows that generally the domain walls run straight from the bottom (γ-Ga_2O_3/sapphire interface) up to the layer surface. Nonetheless, the plane defects identified inside the domains are mostly not perfectly columnar and in the case of the employment of Φ_{SiH_4}, the presence of triangular SiO_x precipitates is found to affect the formation/deviation of them (see blue arrows in Figure 4 for a 17.5 sccm layer). As a result, despite the generally larger width of the rotational domains while increasing the Φ_{SiH_4}, the concentration of plane defects is also suggested to increase (Figure 4).

2.4. Atom Probe Tomography

Since the combined TEM-EDS analysis intrinsically suffers from a large uncertainty in the determination of the Si concentration and its spatial distribution, APT has been performed on two focused ion beam FIB-prepared specimens of samples deposited at Φ_{SiH_4} of 5 and 15 sccm (same layers investigated via TEM-EDS). These specimens were obtained close to the film surfaces, *i.e.*, far from the substrate interface were the γ phase and the presence of SiO_x precipitates was identified by TEM investigation (Figure 4). The TEM dark field images of the two analyzed APT specimens displayed in **Figure 5** show a larger density of straight defects for the 5 sccm with respect to the 15 sccm Φ_{SiH_4}, reasonably associated to rotational domain boundary walls. Therefore, these data qualitatively confirm the previous independent TEM investigation (Figure 3). The mass spectra of the whole analyzed volumes via APT allow for quantification of the atomic percentage of Si with respect to Ga, that is found to be 0.54% and 1.02% for Φ_{SiH_4} of 5 and 15 sccm respectively (Figure S8, Supporting Information). These values are well above a minimum detection level of 52 ppm determined using a 95% confidence interval and the method of reference,[52] and generally in good agreement with TEM-EDS data (Figure 3).

To investigate the presence of Si-doping clusters inside the orthorhombic crystal matrix and/or SiO_x precipitates small enough so to be possibly not highlighted by TEM imaging, a silicon nearest neighbor distribution statistical analysis has been performed on both of the APT analyzed samples (Figure S8, Supporting Information). If there were Si-clustering, the nearest neighbor distance of Si atoms from each other would be different than the nearest neighbor distance between a randomized assignments of the atoms. In neither of the two analyzed sample volumes does that appear to be the case, i.e., the Si dopant is evenly spread in the κ-Ga_2O_3 matrix independently of its overall percentage. As already pointed out, this does not appear to be the case for the first 200–400 nm of the doped films (thickness region probed exclusively by the TEM investigation, see Figure 4) where the presence of SiO_x precipitates has

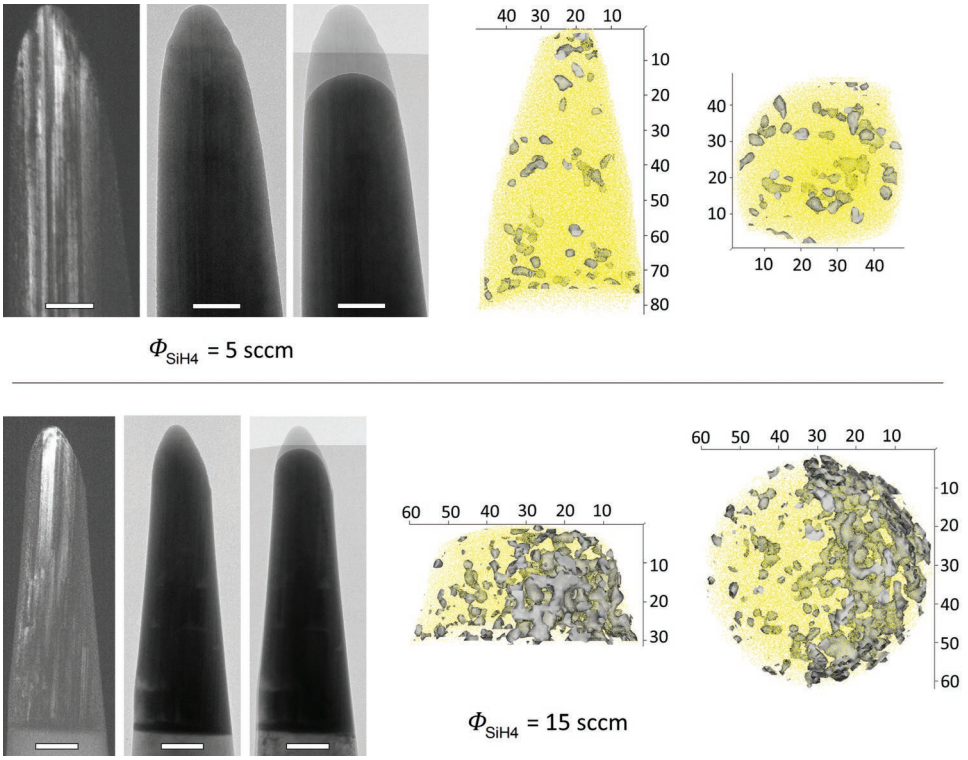

Figure 5. APT investigation of Si-doped κ-Ga_2O_3 layers deposited at Φ_{SiH_4} of 5 and 15 sccm. Dark and bright field TEM images from FIB-prepared APT specimens of samples deposited at Φ_{SiH_4} of 5 and 15 sccm; in the overlay images it is possible to identify the volume removed during APT analysis. The scale bars for the 5 sccm specimen are 50 nm; the scale bars for the 15 sccm specimen are 100 nm. Top and side views of APT reconstructions showing a fraction of the Ga ions in yellow and a 0.4 at% Si isoconcentration surface in gray for the 5 sccm specimen and a 0.6 at% Si isoconcentration surface in gray for the 15 sccm specimen.

already been highlighted. Therefore, different from the qualitative indications coming from EDS line profiling in plan TEM view (Figure 3; Figure S5, Supporting Information), no Si accumulation at defects sites has been highlighted by APT. Nonetheless, just in the 15 sccm sample it has been possible to spot two distinct regions with homogeneous but slightly different Si content, i.e., 0.95% and 1.25% for the low and high concentration sides of the analyzed volume (Figure 5). It is reasonable to assume that such variation could be related to a slightly different content of Si in adjacent orthorhombic domains.

2.5. Raman Spectroscopy

Undoped and doped κ-Ga_2O_3 layers were further analyzed by confocal Raman spectroscopy in back-scattering geometry from the sample surface and edge. Surface back-scattering measurements were performed on all the samples investigated by TEM and APT ($\Phi_{SiH_4} = 0, 5, 15, 17.5$ sccm), with two different laser wavelengths (633 and 532 nm, with the first being the one reported in Figure S9, Supporting Information), producing similar results. Cross-sectional (edge) measurements were performed on the same $\Phi_{SiH_4} = 0, 5, 15$ sccm samples and on an additional 10 sccm one, with the 532 nm laser wavelength in parallel polarization to the c-plane. All spectra were collected in the 50–800 cm^{-1} range. Their analysis is performed after air spectrum subtraction, to remove artifacts from its undesired contributions at low Raman shift (60–80 cm^{-1}), and after normalization with respect to the most intense peak from the sapphire substrate (417 cm^{-1}).

Only modes typical of the orthorhombic polymorph of Ga_2O_3 were identified (aside from the ones of the c-plane sapphire),[38] consistent with the XRD and TEM investigations. Despite the different analysis configurations, both surface and edge spectra equivalently highlight similar differences among the analyzed samples, especially when undoped and doped layers are compared (**Figure 6**a; Figure S9a, Supporting Information).

In particular, the peak-fitting analysis of selected peaks in both configurations, suggests the presence of the Si dopant (i.e., from the introduction of a Φ_{SiH_4} during deposition) consistently results in a variation of the intensity ratio among some of the Raman modes (e.g., 82 and 113 cm^{-1}, insets in Figure 6a; Figure S9a, Supporting Information). Noteworthy, the increasing domain size of samples deposited at larger Φ_{SiH_4} (Figure 3) is accompanied by a strong decrease of the Raman peaks' FWHM (Figure 6b,c; Figure S9b,c, Supporting Information). In cross-sectional spectra, where substrate contribution is less prominent and κ-Ga_2O_3 peaks are better resolved, this evidence is stronger (Figure 6). Moreover, the largest reduction of the line width of all phonon modes is observed between the undoped and 5 sccm sample.

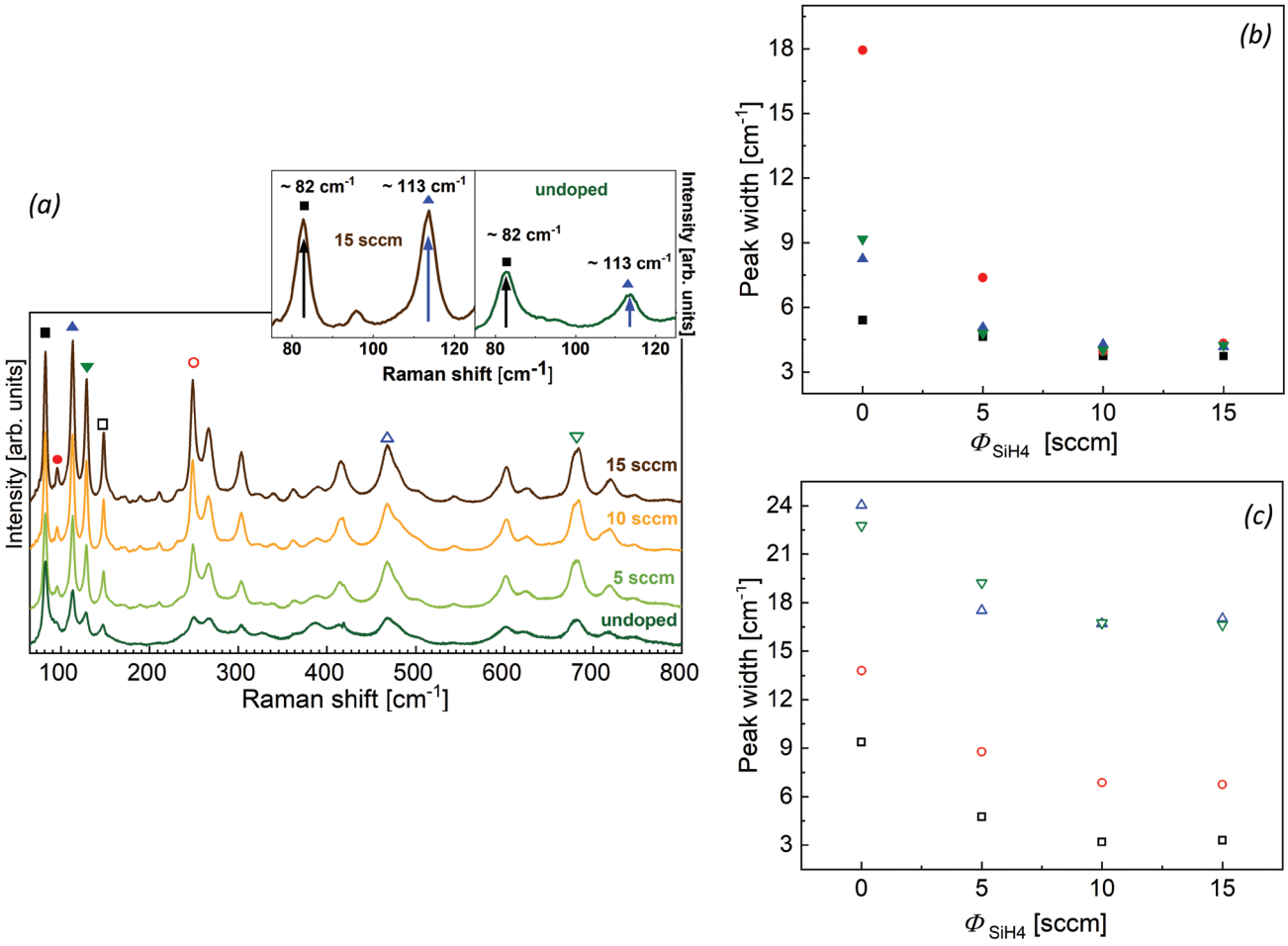

Figure 6. a) Raman spectra in cross sectional (edge) configuration (parallel polarization) of κ-Ga_2O_3 samples deposited at $\Phi_{SiH_4} = 0 - 5 - 10 - 15$ sccm. In the inset the two peaks at ≈ 82 and 113 cm^{-1} are highlighted and compared for the undoped and 15 sccm samples. In b) and c), the fitted peak widths (color/shape correspondence to the symbols reported on the Raman spectra) are reported as a function of the Φ_{SiH_4}; this analysis is performed on selected peaks (i.e., choosing those that are clearly visible in the spectra collected in both configurations, see Figure S9, Supporting Information) and displaced in two separate graphs for sake of clarity.

2.6. Out-of-Plane versus In-Plane Transport Measurements

Finally, to enable a direct measurement on the possible defect-induced (e.g., domains) conductivity anisotropy in epitaxial κ-Ga_2O_3 thin films, ≈ 110 and 1100 nm thick, nominally undoped films (i.e., $\Phi_{SiH_4} = 0$) were deposited on top of C-doped and Si-doped GaN epitaxial templates on c-plane sapphire substrates (insulating and conducting templates, respectively; XRD reported in Figure S10, Supporting Information). The MOVPE chamber has been conditioned before the deposition of these layers so to avoid the possible role of Si unintentional incorporation after growth runs in presence of Φ_{SiH_4} (potentially leading to lower resistivities, see Supporting Information).

The samples deposited on insulating GaN templates as well as a 590 nm thick layer directly deposited on c-plane sapphire under the very same deposition conditions have been used for the determination of the in-plane transport properties of the κ-Ga_2O_3 layers, resulting in a mean $\rho_{in-plane}$ of ≈ 8×10^4 Ωcm (measurements performed on similar TLM contact structures, see Figure S11, Supporting Information).

To measure the out-of-plane transport, squared mesa structures of κ-Ga_2O_3 with well-defined geometries (200 × 200 – 150 × 150 – 100 × 100 – 70 × 70 μm^2, height equal to the κ-Ga_2O_3 layer thicknesses, i.e., 1100 and 110 nm) were then isolated via dry etching on semiconducting GaN templates ($R_{S,GaN} = 66 \frac{\Omega}{sq}$., μ_{GaN} = 217 $cm^2V^{-1}s^{-1}$, n_{GaN} = 8.7×10^{18} cm^{-3}). Several mesas for both κ-Ga_2O_3 deposited layer thicknesses (i.e., 1100 and 110 nm) were electrically characterized via 2-point probe configuration. Considering the case of anisotropic resistance, the total area through which the current is supposed to flow during the out of plane measurements is limited by the top contact size (see schematic representation of a mesa structure in **Figure 7**a), i.e., $A_{top\ contact} = 180 \times 180 - 130 \times 130 - 80 \times 80 - 55 \times 55$ μm^2.

As pointed out in Figure 7c, several series contributions add up to the experimentally measured resistance $R_{measured}$, out of which we are interested in the intrinsic out-of-plane resistance ($R_{\kappa-Ga2O3}$) of the κ-Ga_2O_3 mesa. Given the

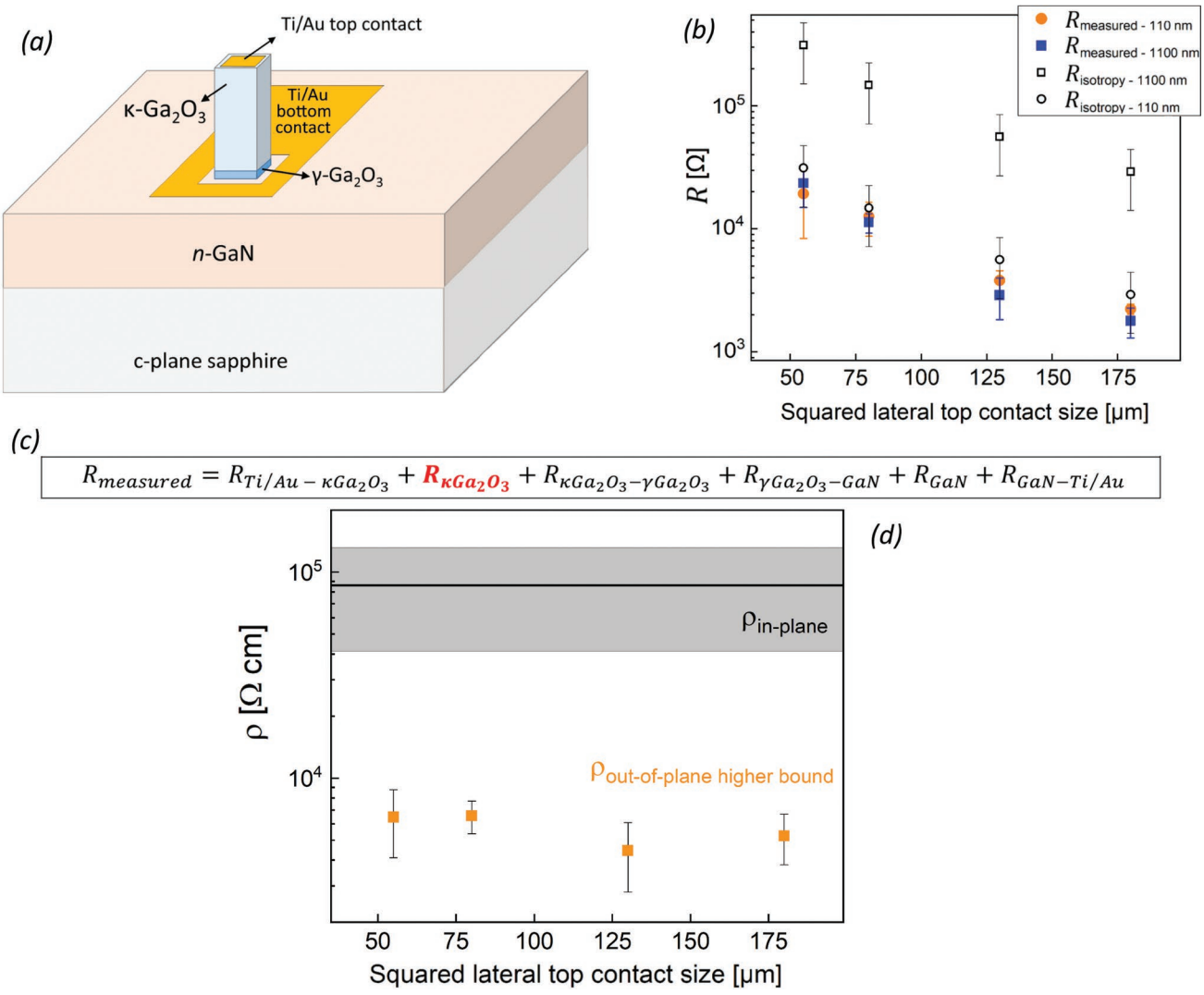

Figure 7. a) Schematic representation (not to scale) of a mesa structure obtained for the κ-Ga_2O_3 thin films deposited on the conductive epitaxial GaN layer. In (b), the experimental out-of-plane $R_{measured}$ (mediated data among several measured mesa structures; full set of data in Figure S12, Supporting Information) as well as the estimated $R_{isotropy}$ (from $\rho_{in-plane}$ measurements, see Figure S11, Supporting Information) are reported for both the investigated κ-Ga_2O_3 thicknesses as a function of the squared lateral top contact size. In (c), the different series resistance contributions embedded in $R_{measured}$ are reported in the current two-terminal probe configuration. In (d), the $\rho_{out-of-plane\ upper\ bound}$ evaluated for the measured mesa structures with different dimensions is reported for the 1100 nm thick κ-Ga_2O_3; in the same graph the straight black line is highlighting the $\rho_{in-plane}$ with the top and bottom lines (gray shaded area) representing the standard deviation (data coming from Figure S11, Supporting Information).

well-defined geometries of the isolated mesas, $R_{\kappa-Ga2O3}$ could be translated into the out-of-plane resistivity, $\rho_{out-of-plane} = (R_{\kappa-Ga2O3}\ A_{top\ contact})/(\kappa-Ga_2O_3$ layer thickness), which can be readily compared to the in-plane resistivity $\rho_{in-plane}$ (evaluated for the material deposited under the very same growth conditions on the insulating GaN templates and sapphire, see Figure S11, Supporting Information). Despite the order of magnitude difference in the two investigated κ-Ga_2O_3 layer thicknesses, the $R_{measured}$ for the different mesa dimensions did not scale, i.e., $R_{measured,\ 1100\ nm} \approx R_{measured,\ 110\ nm}$ (blue squares and orange circles respectively in Figure 7b). This evidence points toward the series resistances being dominant in the 2-point-probe measurements, i.e., not allowing for a direct determination of $R_{\kappa-Ga_2O_3}$. Notwithstanding, it is unquestionable that $R_{measured}$ provides an upper-bound estimate for $R_{\kappa-Ga_2O_3}$, i.e., $R_{\kappa-Ga_2O_3} < R_{measured}$.

Therefore, $R_{measured}$ can be used to provide the upper-bound estimate of the out-of-plane resistivity, i.e., $\rho_{out-of-plane\ upper\ bound} = (R_{measured}\ A_{top\ contact})/(\kappa-Ga_2O_3$ layer thickness) $> \rho_{out-of-plane}$. Figure 7d compares the resulting upper-bound estimate $\rho_{out-of-plane\ upper\ bound}$ for the 1100 nm thick κ-Ga_2O_3 film (i.e., being limited by the series resistances in this estimate) to the $\rho_{in-plane}$, giving a lower bound estimate for the transport anisotropy. It is therefore experimentally found that the out-of-plane resistivity

is at least one order of magnitude lower with respect to the in-plane resistivity in such κ-Ga_2O_3 layers.

3. Discussion

The size of the 120° rotated orthorhombic domains in (001) κ-Ga_2O_3 epitaxial layers on c-plane sapphire substrates (Figure 1) is usually limited to 5–20 nm width. Our results showed that the addition of a silane flow Φ_{SiH_4} during the MOVPE deposition results in *n*-type Si extrinsic doping while at the same time helping to increase the domain size by more than one order of magnitude (Figure 3), both of them contributing to a clear decrease of in-plane resistivity $\rho_{in-plane}$ and increase of in-plane electron mobility μ (Figure 2a,b). The reason behind the domain size control in κ-Ga_2O_3 samples as a function of the Φ_{SiH_4} could be related to a silane-induced increase of the surface mobility of the adsorbed species during the growth process (especially during nucleation of the orthorhombic phase). In the MOVPE growth of Ga_2O_3 with TMG metallorganic precursor and H_2 as gas carrier, hydrogen is supposed to replace the leaving methane resulting in GaH to be adsorbed on the surface.[53] The oxidizing agent (i.e., H_2O in this study) was provided in excess with respect to the TMG flow. Several Ga-O clusters could then possibly form and diffuse on the growth surface (i.e., Ga_2O_2, GaO_4, GaO_3, GaO_2, and GaO), some of which might also desorb (e.g., Ga_2O), although in H_2O excess the latter desorption should not play an important role.[53] In the MOVPE deposition of κ-Ga_2O_3 the growth temperature can not usually exceed 650 °C in order to prevent the stabilization of the monoclinic β polymorph (i.e., T_g can be just varied on a narrow window to increase the surface mobility).[19] Our samples were deposited at the same $\mathbf{T_g}$ = 610 °C and TMG/H_2O flow ratio, and the employment of various Φ_{SiH_4} was the only tuned parameter. A precise discussion of the growth process (e.g., unambiguous identification of the mobile adsorbed species on the surface during growth, role of the surface they are diffusing and nucleating on, i.e., c-plane sapphire or γ-Ga_2O_3, see Figure 4) would require a dedicated study that is out of the scope of this article. Nevertheless, based on the presented results, it is reasonable to assume that silane could be capable of increasing the mobility of the adsorbed species on the growth surface, resulting in an overall lower density of nuclei. This could be triggered by Si or SiH_x accumulating on the surface during growth and preventing in this way the formation of critical size nuclei, i.e., resulting in an increasing diffusion length of the adsorbed species. Such a mechanism has already been proposed for the growth of GaN nanorods by MOCVD in the presence of silane[54] and could qualitatively explain the increasing domain size in κ-Ga_2O_3 while increasing Φ_{SiH_4} (Figure 3). The partial incorporation of Si is also suggested by the APT-measured Si concentration on the two samples deposited with a threefold different Φ_{SiH_4} (5 and 15 sccm) resulting in a just twofold different Si concentration in the probed volume (0.54% and 1.02%, respectively see Figure S8, Supporting Information). On the other hand, the growth rate of the layers remained unaltered with respect to the Φ_{SiH_4}.

In this framework, we could also interpret the presence of the SiO_x precipitates highlighted in the first 200–400 nm of the samples deposited in the presence of a Φ_{SiH_4} (Figure 4). Since the Φ_{SiH_4} is continuously provided during growth, once it overcame a critical density on the surface, this could result in the precipitation of SiO_x inclusions (see HRSTEM, HAADF images and EDS maps in Figure S7, Supporting Information) in the κ-Ga_2O_3 matrix. The precipitates are amorphous and characterized by a not perfectly triangular shape (HRTEM micrographs reported in Figure 4), with their flat side being mostly parallel to the substrate/surface, and their size and density being related to the Φ_{SiH_4}. In particular, larger silane flows result in higher density of smaller triangular precipitates (Figure 4). Nonetheless, the SiO_x precipitates being just limited to the region close to the substrate surface remains an open point that requires further dedicated investigations (TEM, Figure 4; APT, Figure 5).

The electrical properties of the κ-Ga_2O_3 layers are affected by the addition of the Φ_{SiH_4} during growth for a threefold reason: i) Si being a shallow donor in this material system,[29] ii) the domain walls and iii) structural (e.g., plane defects) as well as compensation/self-compensation defects both playing a role in limiting the in-plane electronic conduction. Regarding i), the presented results suggest that not only Si, but also H is likely to play the role of a shallow donor in κ-Ga_2O_3, since the nominally undoped layers ($\Phi_{SiH_4} = 0$) deposited with H_2 as a carrier gas show an in-plane room temperature ρ in the order of 10^3-10^4 Ωcm (Figure 2a; Figure S11, Supporting Information). It should be noted that different MOVPE synthesis parameters (TMG/H_2O flux ratios, H_2 carrier gas flows, and especially the use of different gas carriers, e.g., He)[55] can result in much higher resistivities for layers deposited without Φ_{SiH_4} ($\rho \geq 10^7$ Ωcm).[28] In all the deposited layers the trend of ρ in T (Figure S3, Supporting Information) is suggested to be ruled by a variable range hopping transport (VRH, see Figure S3 and related discussion in the Supporting Information). Nonetheless, the RT ρ is found to decrease while increasing Φ_{SiH_4} during the deposition (Figure 2a). In particular, a significant drop of ρ is recorded up to Φ_{SiH_4}, while afterward its value seems to go toward saturation being mostly scattered around mid-to-low 10^{-1} Ωcm. While ii) the domain size is found to significantly increase together with the silane flow at least up to Φ_{SiH_4} = 15 sccm (Figure 3), it is reasonable to assume that the iii) disorder—i.e., compensation/self-compensation and/or plane defects—would also increase. The occurring ρ saturation could be related to these two competing effects. Particularly, together with the rotational domain size increase with Φ_{SiH_4}, the SiO_x precipitates are also increasing in density, with the latter also interacting with plane defects (Figure 4). The precipitates/plane defects and possible (self-) compensation effects can both contribute to increase the disorder, in turn possibly affecting the VRH transport mechanism.

Also non-uniform Si distribution could play a role in the electronic transport. TEM-EDS line profiles seem to suggest possible Si accumulation at defects interfaces (i.e., both domain walls and plane defects, see Figure 3; Figure S5, Supporting Information). On the other hand, the more sensitive and spatially resolved APT technique excluded the presence of Si inhomogeneities/aggregates in presence of defects in the analyzed volumes (i.e., close to the surface of the deposited films, see Figure 5; Figure S8, Supporting Information). Nonetheless, APT performed on a layer deposited at relatively high Φ_{SiH_4}

(15 sccm) reveals local Si concentration differences (e.g., 0.95% and 1.25%, Figure 5) that have been attributed to different domains, although the Si concentrations are homogeneously distributed inside the domains themselves (Figure S8, Supporting Information).

In the Hall effect characterization (Figure 2b,c), the Hall voltage must be handled with caution in the case of hopping conduction.[45] The experimental Hall density n is related to the density of donor sites $N_s(T)$ taking part to the hopping process, which is usually considered evenly distributed over the film thickness. Surprisingly, it is here reported that n tends to decrease while increasing Φ_{SiH_4} (Figure 2c). A n reduction implies an increased compensation and/or a reduction of the donor sites. An effect of reduction of effective thickness of the conductive channel due to the SiO_x precipitates (Figure 4; Figure S7, Supporting Information) and possible depleted regions around them, even if possible, cannot explain a reduction of the Hall density of a factor of about five (Figure 2c). Differently, the mobility μ increase (Figure 2b) would not be affected by the eventual overestimation of the conduction channel; therefore, this should be related to a rising hopping probability which can be qualitatively associated with the widening of the domains.

The Hall-effect absolute values of n should be interpreted with caution in this particular case (i.e., VRH transport mechanism and not well-defined thickness of the conductive channel). Nonetheless, a comparison among the extracted n and the APT measurements (Figure 2c; Figure S8, Supporting Information) allows to highlight a high level of compensation. For example, the APT measured layer deposited at 15 sccm Φ_{SiH_4} is characterized by a Si concentration of ≈ 1%. For a full dopant activation efficiency (i.e., all Si being incorporated in the correct Ga substitutional site and neglecting compensation), this would correspond to a charge carrier density of about mid 10^{20} cm^{-3}, while the collected Hall measurements suggest n being in the order of 2×10^{18} cm^{-3}. This could be driven by a) charge compensation related to the presence of electrically active plane defects/domain boundaries and/or to a large concentration of deep acceptors (e.g., Ga vacancies V_{Ga}), and b) by the incorporation of Si in sites different from the Ga substitutional ones (e.g., interstitial, or as SiO_x precipitates as highlighted in the first 200–400 nm of the doped layers). In (a), also a self-passivation mechanism once overcoming a certain E_F level (e.g., a threshold Si concentration) resulting in the favorable formation of deep acceptor defects (e.g., V_{Ga}) to maintain the crystal charge neutrality could be considered, like in the case of the β-Ga_2O_3 polymorph.[56] In light of the VRH transport, a significant increase of compensating defects while increasing the Φ_{SiH_4} can have detrimental effects on the density of hopping carriers, while the hopping mobility could be mostly beneficially affected by the concurring increase of the domain size. This simplified picture could explain the puzzling behavior of Hall density and mobility with the silane flow. In this direction, it is worth mentioning that the κ-Ga_2O_3 material system has not been yet thoroughly investigated due to the limited reports in doped semiconducting layers[28] and complicated interplay between defects and conduction mechanism.[29]

Indeed, the tightly bonded interplay between vertically oriented structural defects (i.e., domains and plane defects) and electronic conduction results in the experimentally demonstrated defect-driven conduction anisotropy in (001) epitaxial κ-Ga_2O_3 layers. In particular, the data reported in this work quantitatively show an at least (lower estimate due to series resistances, see Figure 7) one order of magnitude higher in-plane resistivity (i.e., charge carriers crossing domain interfaces) than out-of-plane resistivity (i.e., charge carriers flowing along the vertically oriented domains), in line with previously reported qualitative experimental data.[30] In this framework it is important to stress out that theoretical[50,57] and experimental[29] works on κ-Ga_2O_3 as well as the comparison among similarly structurally anisotropic oxides (e.g., β-Ga_2O_3[58] and SnO_2[59]) exclude the possibility that the extent of this highlighted (lower bound) anisotropy could be possibly related to the pure orthorhombic structure of Ga_2O_3. The measurements here reported have been performed on nominally undoped samples ($\Phi_{SiH_4} = 0$, maximum domain dimension around 20 nm, see Figure 3) deposited on GaN templates; this has been done to avoid the presence of SiO_x precipitates (confined in the first 200–300 nm close to the substrate interface in layers deposited with Φ_{SiH_4}, see Figure 4) that could potentially interfere in the out-of-plane R measurements. The demonstrated defects-driven anisotropy in the κ-Ga_2O_3 material system is most likely the reason that so far prevented the isolation of 2DEGs in κ-Ga_2O_3/$Al_xGa_{2-x}O_3$ heterostructures,[23] and more generally so far inhibited the application of this material system in the field of power electronics. The deep understanding of the growth process and the employment of proper substrates[26,27] will soon together open the attainment of single domain κ-Ga_2O_3 semiconducting layers with tunable electrical properties.

As pointed out, the characterization of the domain structure—i.e., both their presence and typical associated width—is fundamental for the κ-Ga_2O_3 epitaxial layers. Therefore, it is important to highlight the thorough non-destructive structural characterization here proposed via XRD and Raman spectroscopy. At first, the significantly reduced FWHM in the XRD ω-scans of the out-of-plane (004) reflection as a function of the Φ_{SiH_4} (Figure 1c) highlights its clear relation with the different orthorhombic domain size in these samples. Moreover, the RSM measurements in the vicinity of the (122) reflection confirmed the possibility of getting qualitative information at least on very different domain size distributions (i.e., from < 20 nm to > 100 nm wide passing from $\Phi_{SiH_4} = 0$ to > 5 sccm, respectively, see Figure S2, Supporting Information). It should be noted that the [122] direction is ≈54° away from the surface normal, so a relevant component of the scattering vector is in-plane. In this light both the different ω and 2θ FWHM extracted values (Table S1, Supporting Information) significantly decreased when the Φ_{SiH_4} was introduced during growth. Particularly, the smaller FWHM values in the 2θ direction indeed can be directly linked to the increased mean crystallite size, in agreement with TEM characterization (Figure 3; Figure S4, Supporting Information). Nonetheless, it should be also considered that the 2θ FWHM could be as well related to strain and/or microstructural effects. In this framework it is difficult to evaluate the role of the inhomogeneously distributed SiO_x precipitates (just limited to the region close to the substrate surface as highlighted by TEM—Figure 4—and

APT—Figure S8, Supporting Information) with size and concentration being a function of the Φ_{SiH_4}.

Finally, a clear indication of increasing mean domain size is independently provided also by Raman spectroscopy. In particular, the consistent trend of the Raman peaks narrowing highlighted in both confocal and cross-sectional configurations (Figure 6; Figure S9, Supporting Information) may be generally related to phonon lifetimes being affected by the different domain sizes of the investigated layers. More in detail, phonons in the samples with the smallest domains of ≈ 5–20 nm (i.e., no Φ_{SiH_4}) are significantly affected by boundary scattering at the domain wall, resulting in a reduction of the phonon mean free path and phonon lifetimes. Consequently, the Raman modes experience a significant line width broadening. Upon silane introduction, the increased domain size reduced the contributions of domain boundary scattering, thus a strong reduction in the Raman line width is observed (see Figure 6b,c; Figure S9b,c, Supporting Information). The effect becomes less significant for even larger domains > 100 nm (i.e., Φ_{SiH_4} > 5 sccm) as other scattering mechanisms contribute to the limitation of the phonon lifetimes. Moreover, Raman has also shown high potential for the investigation of the dopant role in this material system, i.e., intensity change of specific peaks (e.g., 82 and 113 cm^{-1}, see insets in Figure 6a; Figure S9a, Supporting Information). This aspect should be further investigated in a dedicated work.

4. Conclusions

The rotational domain size is among the major issues affecting the in-plane electronic transport in κ-Ga_2O_3, a polymorph with significant, but so far unrealized potential in the field of new generation power electronics. In this framework, the ability to control their size upon silane-mediated growth demonstrated in this work (i.e., from about tens to about hundreds of nanometers) represents a fundamental step forward for the obtainment of an ultra-wide bandgap material with tailored semiconducting properties. Being of particular significance for this material system, we have here demonstrated and provided experimental guidelines to get fine and qualitative information for the characterization of the domain size distribution in κ-Ga_2O_3 (001)-oriented epitaxial layers with two widely employed and non-destructive characterization techniques, i.e., XRD and Raman spectroscopy. Moreover, in- versus out-of-plane electrical measurements experimentally allowed to measure the defect-mediated lower bound limit of resistivity anisotropy in epitaxial κ-Ga_2O_3 layers. In particular, the out-of-plane resistivity has been found to be at least one order of magnitude lower than the in-plane resistivity. This i) once more highlights the detrimental role of domains in κ-Ga_2O_3 while ii) suggests that their enlargement/suppression together with the limitation of plane and compensation defects—is of paramount importance to improve and tailor the in-plane conduction, therefore highlighting the full potential of this material. Moreover, the thorough characterization of a domain structured epilayer here proposed is of wider relevance considering different material systems where such structural defects rule the resulting functional properties.

5. Experimental Section

The κ-Ga_2O_3 layers were grown by MOVPE at a partial pressure of 60 mbar and substrate temperature T_g = 610 °C on nominally oriented c-plane sapphire substrates. Trimethylgallium (TMG) and ultrapure H_2O stored in dedicated stainless-steel bubblers at 1 and 30 °C respectively, were used as metal precursor and oxidizing gas. H_2 was used as gas carrier with a flow of 2000 standard cubic centimeters per minute (sccm). The ratio of the precursors pressures (p_{H2O}/p_{TMG} ≈ 350), as well as the deposition time (t_{dep} = 100 min, resulting in ≈ 800–900 nm thick layers determined using a Jasco UV–vis V-530 spectrophotometer[60]) had been both kept constant for all the growth runs. Different flows of an H_2-diluted mixture of 0.05% SiH_4 were provided while maintaining the other synthesis parameters in different growth runs (Φ_{SiH_4} from 0 to 17.5 sccm, where Φ_{SiH_4} refers to the H_2-diluted SiH_4 mixture). The investigated ratio between the partial pressure of effective SiH_4 and partial pressure of TMG (p_{SiH4}/p_{TMG}) ranged from 0 to ≈ 8.7×10^{-2}.

The deposited layers were characterized by XRD using a Rigaku Smartlab XE diffractometer with CuK_α wavelength, equipped with cross beam optics unit to achieve parallel beam geometry, Eulerian cradle and HyPix3000 detector. Symmetric out-of-plane 2θ-θ and ω rocking curves as well as φ-scans on asymmetric reflections were performed to get information on the crystal quality and domain structure of the orthorhombic κ-Ga_2O_3 layers.[37] Reciprocal space mapping (RSM) had been performed in order to qualitatively investigate the mean size of the columnar domains among samples deposited with different Φ_{SiH_4}. Confocal Raman spectroscopy measurements were obtained using a Horiba LabRAM HR Evolution confocal spectrometer (focal 800 mm), using a configuration with a 600 lines mm^{-1} grating, a set of Bragg ultra-low frequency filters for the rejection of the Rayleigh scattering and a liquid nitrogen-cooled CCD detector. The 633 and 532 nm laser lines were used for excitation (P < 1 mW). An optical 100x objective was used to obtain a spatial resolution of ≈ 1 µm, with 0.5 cm^{-1} resolution. Typical collection time for the confocal configuration was 60 s for each acquisition, with 10 repetitions. Additional measurements in cross-sectional configuration[38] with a λ = 532 nm were performed with another LabRAM HR 800 spectrometer (Horiba Jobin-Yvon).

The (scanning) transmission electron microscopy (TEM) was carried out in an aberration corrected Thermo Fischer Scientific THEMIS microscope at 200 keV on selected samples. The cross-sectional TEM samples were prepared by focused ion beam (FIB) technique. The plan view TEM samples were prepared by conventional Ar-ion beam milling. For the energy dispersive X-ray spectroscopy (EDS) mapping a Super-X detector was used in STEM mode. In order to get quantitatively reliable information on the amount of Si (N_{Si}) in this layers and its distribution with a nanometric scale resolution, atom probe tomography (APT) had been employed on two selected samples deposited at different Φ_{SiH_4}. The APT specimens were prepared using a FIB lift-out method in an FEI Helios NanoLab 600i and a Tescan S8252G instrument. The specimens were mounted on tungsten half-grids in holders compatible with the FIB, TEM, and APT instruments.[61] The FIB-prepared APT specimens were analyzed by dark and bright field TEM imaging at 200 keV in an FEI Talos F200X TEM before and after the APT analysis in order to identify and spatially locate the presence of structural defects in the probed volume of the material and assist in generating the reconstructions. Laser pulsed APT analysis was performed in a Cameca LEAP 4000X Si using a 90 mm flight path length at a temperature of 50 K. A laser energy of 40 pJ at repetition rates of 333–500 kHz was used. The detection rate was fixed at 6 ions per 1000 pulses that resulted in a bias range of 3200–6300 V during the analyses. A systematic energy deficit correction was applied to the resulting data to improve the mass spectral resolution by correcting for electrostatic effects.[62] Reconstructions were generated using Cameca's IVAS 3.6.18 software with the TEM images of the specimens before and after analysis providing guidance for constraining the reconstruction parameters.[63]

All the κ-Ga_2O_3 layers were electrically characterized at room temperature (RT) via 4-point probe van der Pauw configuration,

performing resistivity as well as Hall measurements (Keithley Hall-measurement setup, magnetic field of 0.8 T). For a selected number of samples, an additional investigation in the 10–300 K temperature range was performed. For this purpose Ti/Au[28] or SnO_{2-x}/ITO/Au[64] Ohmic contacts were fabricated with a sputtering technique on the corners of squared shaped samples.

Additional κ-Ga_2O_3 layers were deposited on electrically conducting (Si-doped) as well as insulating (C-doped) GaN epitaxial templates on c-plane sapphire substrates, which were deposited according to reference.[65] Ohmic Ti/Au contacts (20 nm/100 nm) with different geometries and spacings had been deposited by electron-beam evaporation and a lift-off process on top of the κ-Ga_2O_3/insulating GaN epitaxial layers to allow in-plane transport measurements through the transfer length TLM method (linear TLM 200 µm wide, gaps: 70, 60, 50, 40, 30, and 20 µm–circular TLM inner contact diameter 80 µm, gap spacing: 5, 10, 15, 25, 50, 75, and 100 µm). A mesa structure with well-defined and isolated κ-Ga_2O_3 squared columns (200 × 200, 150 × 150, 100 × 100, and 70 × 70 μm^2) had been obtained via dry etching processing the samples (inductively couple plasma – reactive ion etching ICP-RIE process details reported in reference,[5] 1.1 nm s^{-1} etch rate for κ-Ga_2O_3) deposited on top of the conducting GaN epitaxial templates. Ohmic Ti/Au contacts had been deposited around the mesa (on the Si:GaN layer) as well as on top of the κ-Ga_2O_3 mesas (180 × 180, 130 × 130, 80 × 80, and 55 × 55 μm^2) so to allow 2-point-probe out-of-plane resistance measurements to provide information on the possible structurally-driven conduction anisotropy (i.e., in- versus out-of-plane) in the material. For this purpose, two different κ-Ga_2O_3 thicknesses (1100 and 110 nm) were tested.

Supporting Information

Supporting Information is available from the Wiley Online Library or from the author.

Acknowledgements

The authors would like to thank Salvatore Vantaggio for helping in the data acquisition and experimental setup of the electrical measurements (University of Parma), and Sander Rauwerdink and Andreas Walid for sample processing (Paul Drude Institute of Berlin). Work by O.B. and A.T. was performed in the framework of GraFOx, a Leibniz-science Campus pasrtially funded by the Leibniz association. This research has financially been supported by the Programme "FIL - Quota Incentivante" of University of Parma and co-sponsored by Fondazione Cariparma.

Open Access Funding provided by Universita degli Studi di Parma within the CRUI-CARE Agreement.

Conflict of Interest

The authors declare no conflict of interest.

Data Availability Statement

The data that support the findings of this study are available in the supplementary material of this article.

Keywords

gallium oxides, rotational domains, semiconducting oxides, structural and point defects, thin films epitaxy, transport anisotropy

Received: July 8, 2022
Revised: September 20, 2022
Published online: November 7, 2022

[1] M. Higashiwaki, K. Sasaki, A. Kuramata, T. Masui, S. Yamakoshi, *Appl. Phys. Lett.* **2012**, *100*, 013504.
[2] S. J. Pearton, J. Yang, P. H. Cary, F. Ren, J. Kim, M. J. Tadjer, M. A. Mastro, *Appl. Phys. Rev.* **2018**, *5*, 011301.
[3] R. Roy, V. G. Hill, E. F. Osborn, *J. Am. Chem. Soc.* **1952**, *74*, 719.
[4] M. Baldini, Z. Galazka, G. Wagner, *Wide Band Gap Semicond. Technol. Gener. Energy Effic. Power Electron.* **2018**, *78*, 132.
[5] M. Budde, D. Splith, P. Mazzolini, A. Tahraoui, J. Feldl, M. Ramsteiner, H. von Wenckstern, M. Grundmann, O. Bierwagen, *Appl. Phys. Lett.* **2020**, *117*, 252106.
[6] S. Fujita, K. Kaneko, *Proc. 17th Int. Conf. Cryst. Growth Epitaxy ICCGE-17* **2014**, *401*, 588.
[7] E. G. Villora, K. Shimamura, K. Kitamura, K. Aoki, *Appl. Phys. Lett.* **2006**, *88*, 031105.
[8] M. Orita, H. Ohta, M. Hirano, H. Hosono, *Appl. Phys. Lett.* **2000**, *77*, 4166.
[9] P. Mazzolini, O. Bierwagen, *J. Phys. D: Appl. Phys.* **2020**, *53*, 354003.
[10] P. Mazzolini, A. Falkenstein, Z. Galazka, M. Martin, O. Bierwagen, *Appl. Phys. Lett.* **2020**, *117*, 222105.
[11] R. Schewski, K. Lion, A. Fiedler, C. Wouters, A. Popp, S. V. Levchenko, T. Schulz, M. Schmidbauer, S. Bin Anooz, R. Grüneberg, Z. Galazka, G. Wagner, K. Irmscher, M. Scheffler, C. Draxl, M. Albrecht, *APL Mater.* **2018**, *7*, 022515.
[12] K. Sasaki, A. Kuramata, T. Masui, E. G. Víllora, K. Shimamura, S. Yamakoshi, *Appl. Phys. Express* **2012**, *5*, 035502.
[13] E. Ahmadi, O. S. Koksaldi, X. Zheng, T. Mates, Y. Oshima, U. K. Mishra, J. S. Speck, *Appl. Phys. Express* **2017**, *10*, 071101.
[14] A. Fiedler, R. Schewski, M. Baldini, Z. Galazka, G. Wagner, M. Albrecht, K. Irmscher, *J. Appl. Phys.* **2017**, *122*, 165701.
[15] S. Rafique, L. Han, A. T. Neal, S. Mou, J. Boeckl, H. Zhao, *Phys. Status Solidi A* **2018**, *215*, 1700467.
[16] P. Mazzolini, P. Vogt, R. Schewski, C. Wouters, M. Albrecht, O. Bierwagen, *APL Mater.* **2018**, *7*, 022511.
[17] P. Mazzolini, A. Falkenstein, C. Wouters, R. Schewski, T. Markurt, Z. Galazka, M. Martin, M. Albrecht, O. Bierwagen, *APL Mater.* **2020**, *8*, 011107.
[18] Z. Guo, A. Verma, X. Wu, F. Sun, A. Hickman, T. Masui, A. Kuramata, M. Higashiwaki, D. Jena, T. Luo, *Appl. Phys. Lett.* **2015**, *106*, 111909.
[19] M. Bosi, P. Mazzolini, L. Seravalli, R. Fornari, *J. Mater. Chem. C* **2020**, *8*, 10975.
[20] F. Mezzadri, G. Calestani, F. Boschi, D. Delmonte, M. Bosi, R. Fornari, *Inorg. Chem.* **2016**, *55*, 12079.
[21] P. Ranga, S. B. Cho, R. Mishra, S. Krishnamoorthy, *Appl. Phys. Express* **2020**, *13*, 061009.
[22] S. B. Cho, R. Mishra, *Appl. Phys. Lett.* **2018**, *112*, 162101.
[23] M. Kneiß, P. Storm, A. Hassa, D. Splith, H. von Wenckstern, M. Lorenz, M. Grundmann, *APL Mater.* **2020**, *8*, 051112.
[24] I. Cora, F. Mezzadri, F. Boschi, M. Bosi, M. Čaplovičová, G. Calestani, I. Dódony, B. Pécz, R. Fornari, *Cryst. Eng. Comm.* **2017**, *19*, 1509.
[25] M. Kneiß, A. Hassa, D. Splith, C. Sturm, H. von Wenckstern, T. Schultz, N. Koch, M. Lorenz, M. Grundmann, *APL Mater.* **2018**, *7*, 022516.
[26] H. Nishinaka, O. Ueda, D. Tahara, Y. Ito, N. Ikenaga, N. Hasuike, M. Yoshimoto, *ACS Omega* **2020**, *5*, 29585.
[27] Y. Zhang, Y. Gong, X. Chen, Y. Kuang, J. Hao, F.-F. Ren, S. Gu, R. Zhang, J. Ye, *ACS Appl. Electron. Mater.* **2022**, *4*, 461.
[28] A. Parisini, A. Bosio, V. Montedoro, A. Gorreri, A. Lamperti, M. Bosi, G. Garulli, S. Vantaggio, R. Fornari, *APL Mater.* **2019**, *7*, 031114.
[29] H. J. von Bardeleben, J. L. Cantin, A. Parisini, A. Bosio, R. Fornari, *Phys. Rev. Mater.* **2019**, *3*, 084601.
[30] M. Kneiß, D. Splith, P. Schlupp, A. Hassa, H. von Wenckstern, M. Lorenz, M. Grundmann, *J. Appl. Phys.* **2021**, *130*, 084502.

[31] A. Parisini, P. Mazzolini, O. Bierwagen, C. Borelli, K. Egbo, A. Sacchi, M. Bosi, L. Seravalli, A. Tahraoui, R. Fornari, *J Vac Sci Technol A* **2022**, *40*, 042701.
[32] M. Grundmann, T. Böntgen, M. Lorenz, *Phys. Rev. Lett.* **2010**, *105*, 146102.
[33] W. Wang, L. Li, J. Liu, B. Chen, Y. Ji, J. Wang, G. Cheng, Y. Lu, G. Rijnders, G. Koster, W. Wu, Z. Liao, *npj Quantum Mater.* **2020**, *5*, 73.
[34] A. Bartasyte, S. Margueron, T. Baron, S. Oliveri, P. Boulet, *Adv. Mater. Interfaces* **2017**, *4*, 1600998.
[35] S. Kaufmann, R. Niemann, T. Thersleff, U. K. Rößler, O. Heczko, J. Buschbeck, B. Holzapfel, L. Schultz, S. Fähler, *New J Phys* **2011**, *13*, 053029.
[36] Z. Chen, Z. Luo, Y. Qi, P. Yang, S. Wu, C. Huang, T. Wu, J. Wang, C. Gao, T. Sritharan, L. Chen, *Appl. Phys. Lett.* **2010**, *97*, 242903.
[37] H. Nishinaka, H. Komai, D. Tahara, Y. Arata, M. Yoshimoto, *Jpn. J. Appl. Phys.* **2018**, *57*, 115601.
[38] B. M. Janzen, P. Mazzolini, R. Gillen, V. F. S. Peltason, L. P. Grote, J. Maultzsch, R. Fornari, O. Bierwagen, M. R. Wagner, *J. Mater. Chem. C* **2021**, *9*, 14175.
[39] J. E. N. Swallow, C. Vorwerk, P. Mazzolini, P. Vogt, O. Bierwagen, A. Karg, M. Eickhoff, J. Schörmann, M. R. Wagner, J. W. Roberts, P. R. Chalker, M. J. Smiles, P. Murgatroyd, S. A. Razek, Z. W. Lebens-Higgins, L. F. J. Piper, L. A. H. Jones, P. K. Thakur, T.-L. Lee, J. B. Varley, J. Furthmüller, C. Draxl, T. D. Veal, A. Regoutz, *Chem. Mater.* **2020**, *32*, 8460.
[40] M. Kneiß, A. Hassa, D. Splith, C. Sturm, H. von Wenckstern, M. Lorenz, M. Grundmann, *APL Mater.* **2019**, *7*, 101102.
[41] Y. Oshima, E. G. Víllora, Y. Matsushita, S. Yamamoto, K. Shimamura, *J. Appl. Phys.* **2015**, *118*, 085301.
[42] X. Xia, Y. Chen, Q. Feng, H. Liang, P. Tao, M. Xu, G. Du, *Appl. Phys. Lett.* **2016**, *108*, 202103.
[43] V. I. Nikolaev, S. I. Stepanov, A. I. Pechnikov, S. V. Shapenkov, M. P. Scheglov, A. V. Chikiryaka, O. F. Vyvenko, *ECS J. Solid State Sci. Technol.* **2020**, *9*, 045014.
[44] P. Vogt, O. Brandt, H. Riechert, J. Lähnemann, O. Bierwagen, *Phys. Rev. Lett.* **2017**, *119*, 196001.
[45] N. F. Mott, E. A. Davis, *Electronic processes in non-crystalline materials*, 2nd ed., Clarendon Press, Oxford **2012**.
[46] F. Tremblay, M. Pepper, D. Ritchie, D. C. Peacock, J. E. F. Frost, G. A. C. Jones, *Phys. Rev. B* **1989**, *39*, 8059.
[47] N. F. Mott, *Metal-insulator transitions*, 2nd ed., Taylor & Francis, London; New York **1990**.
[48] B. I. Shklovskii, A. L. Ėfros, *Electronic properties of doped semiconductors*, 1st ed. Springer, Berlin Heidelberg **2013**.
[49] A. J. Green, J. Speck, G. Xing, P. Moens, F. Allerstam, K. Gumaelius, T. Neyer, A. Arias-Purdue, V. Mehrotra, A. Kuramata, K. Sasaki, S. Watanabe, K. Koshi, J. Blevins, O. Bierwagen, S. Krishnamoorthy, K. Leedy, A. R. Arehart, A. T. Neal, S. Mou, S. A. Ringel, A. Kumar, A. Sharma, K. Ghosh, U. Singisetti, W. Li, K. Chabak, K. Liddy, A. Islam, S. Rajan, et al, *APL Mater.* **2022**, *10*, 029201.
[50] S.-D. Guo, H.-M. Du, *Eur. Phys. J. B* **2020**, *93*, 7.
[51] Q. Liu, Z. Chen, X. Zhou, *ACS Omega* **2022**, *7*, 11643.
[52] D. J. Larson, *Local electrode atom probe tomography: a user's guide*, Springer, New York **2013**.
[53] W. Miller, D. Meiling, R. Schewski, A. Popp, S. B. Anooz, M. Albrecht, *Phys. Rev. Res.* **2020**, *2*, 033170.
[54] J. Z. Li, Z. Z. Chen, S. F. Li, Q. Q. Jiao, Y. L. Feng, S. X. Jiang, Y. F. Chen, T. J. Yu, B. Shen, G. Y. Zhang, *Superlattices Microstruct.* **2016**, *96*, 234.
[55] A. Parisini, A. Bosio, H. J. von Bardeleben, J. Jimenez, S. Dadgostar, M. Pavesi, A. Baraldi, S. Vantaggio, R. Fornari, *Mater. Sci. Semicond. Process.* **2022**, *138*, 106307.
[56] S. Lany, *APL Mater.* **2018**, *6*, 046103.
[57] Z.-C. Zhang, Y. Wu, S. Ahmed, *Mater. Res. Express* **2019**, *6*, 125904.
[58] C. Golz, Z. Galazka, J. Lähnemann, V. Hortelano, F. Hatami, W. T. Masselink, O. Bierwagen, *Phys. Rev. Mater.* **2019**, *3*, 124604.
[59] O. Bierwagen, Z. Galazka, *Appl. Phys. Lett.* **2018**, *112*, 092105.
[60] M. Bosi, L. Seravalli, P. Mazzolini, F. Mezzadri, R. Fornari, *Cryst. Growth Des.* **2021**, *21*, 6393.
[61] B. P. Gorman, D. Diercks, N. Salmon, E. Stach, G. Amador, C. Hartfield, *Microsc. Today* **2008**, *16*, 42.
[62] B. W. Caplins, P. T. Blanchard, A. N. Chiaramonti, D. R. Diercks, L. Miaja-Avila, N. A. Sanford, *Ultramicroscopy* **2020**, *213*, 112995.
[63] D. R. Diercks, B. P. Gorman, *Ultramicroscopy* **2018**, *195*, 32.
[64] A. Bosio, C. Borelli, A. Parisini, M. Pavesi, S. Vantaggio, R. Fornari, *ECS J. Solid State Sci. Technol.* **2020**, *9*, 055002.
[65] S. Leone, R. Fornari, M. Bosi, V. Montedoro, L. Kirste, P. Doering, F. Benkhelifa, M. Prescher, C. Manz, V. Polyakov, O. Ambacher, *J. Cryst. Growth* **2020**, *534*, 125511.